

Spatiotemporal optical vortex (STOV) polariton

M. S. Le, S. W. Hancock, N. Tripathi, and H. M. Milchberg

Institute for Research in Electronics and Applied Physics and Dept. of Physics, University of Maryland, College Park, Maryland 20742, USA

We confirm the existence of the spatiotemporal optical vortex (STOV) polariton and the value of its transverse orbital angular momentum (tOAM), verifying our theory of tOAM in a simple dispersive medium [S. W. Hancock *et al.*, Phys. Rev. Lett. **127**, 193901 (2021)]. We also develop a physical picture of the polariton as a tOAM structure driven by torques induced by the ponderomotive force of the light in the presence of material dispersion. This is a new type of spatiotemporal torque unanticipated in our recent work [S. W. Hancock *et al.*, Phys. Rev. X **14**, 011031 (2024)]. These results are accomplished by high resolution particle-in-cell (PIC) simulations of STOV pulse reflection from and transmission through a fully ionized hydrogen plasma slab. The linear theory matches the PIC simulations up to near-critical plasma densities and near-relativistic field strengths. For higher intensities, optical tOAM becomes invested in collective modes of the plasma.

I. INTRODUCTION

In the past few years, a new form of structured light has been the subject of rapidly increasing research activity: spatiotemporal optical vortices (STOVs), which carry orbital angular momentum (OAM) oriented transverse to propagation, with the associated phase winding and energy density circulation in a spatiotemporal plane [1,2]. This is in contrast with well-known beams carrying longitudinal OAM [3], such as Laguerre-Gaussian modes, whose phase and energy density circulates in spatial degrees of freedom [3].

STOVs were first observed as emergent toroidal electromagnetic (EM) structures, akin to “smoke rings” threaded by the propagation axis, initiated by the extreme spatiotemporal phase shear accumulated during arrested self-focusing collapse of intense femtosecond pulses in air [1]. STOVs have been shown to be necessary and universal structures that mediate EM energy flow in intense propagating pulses over widely different intensity regimes, from nonrelativistic filamentation in Kerr media to relativistic filamentation in plasmas [1,4]. As they are carried by pulses, STOVs are necessarily polychromatic [5]. The generation of STOVs by spatiotemporal phase shear led to the realization that one could generate freely propagating STOVs by first applying phase shear in the spatio-spectral domain using a $4f$ pulse shaper [6–8] and then returning the pulse to the spatiotemporal domain. Other efforts followed using this technique [9,10] with still others exploring the use of metasurfaces [11,12]. Further experiments demonstrating transverse OAM (tOAM) conservation in second harmonic generation provided confirmation that tOAM can be carried by photons [9,13].

In parallel with our experimental work, we developed a linear theory of mode structure and tOAM of STOVs in dispersive media that predicted half-integer intrinsic tOAM and the existence of a quasiparticle we called a “STOV polariton”, which embodies the tOAM-carrying material

response [2]. For nondispersive media, the theory is in excellent agreement with measurements of freely propagating STOVs in air [2] and experiments measuring the tOAM transfer by spatiotemporal perturbations on general light pulses, a process we dubbed “spatiotemporal torquing of light” [14,15]. However, investigating the validity of the tOAM theory in a dispersive medium remained an unfinished task.

In this paper, we verify our tOAM theory in a simple dispersive medium, confirming the existence of the STOV polariton and the value of its tOAM. We also develop a physical picture of the polariton as a tOAM structure driven by torques induced by the ponderomotive force of the light in the presence of material dispersion. This is a new type of spatiotemporal torque unanticipated in our recent work [14]. To accomplish these results, we use high resolution particle-in-cell (PIC) simulations of a slab of fully ionized, collisionless hydrogen plasma, directly tracking the tOAM of the particles and fields. There are two main advantages of this approach: (1) There are no assumptions about material response, such as constitutive relations or dispersion relations; only Maxwell’s equations and the Lorentz force are used. (2) A PIC simulation can explore the plasma response from the linear through the highly nonlinear regime, enabling an assessment of the validity range of our theory. We find that increasing the laser pulse intensity beyond a threshold set by the plasma density results in deviation from the linear theory, as tOAM becomes invested in collective modes of the plasma.

II. THEORETICAL BACKGROUND AND SIMULATIONS

Our linear theory is briefly reviewed in Appendix A, where several parameters used in the rest of this paper are introduced. One solution of the theory’s spatiotemporal paraxial wave equation (A1) is a STOV pulse with transverse orbital angular momentum. In vacuum or in media with negligible dispersion, the simplest STOV pulse with winding number or topological charge l ($0, \pm 1, \pm 2, \dots$) has the following form near its waist for $z/z_{0x} \ll 1$ and $z/z_{0y} \ll 1$ [2],

$$A_{l,\alpha}(x, y, \xi; z = 0) = A^{(0)} \left(\frac{\xi}{w_{0\xi}} \pm \frac{ix}{w_{0x}} \right)^{|l|} e^{-(x^2/w_{0x}^2 + y^2/w_{0y}^2)} e^{-\xi^2/w_{0\xi}^2}, \quad (1)$$

where the various parameters are defined in Appendix A. Here, we take the tOAM to be directed along y , $\{w_{0x}, w_{0y}, w_{0\xi}\}$ are scale widths of the pulse along $\{x, y, \xi\}$, $z_{0x} = \frac{1}{2}kw_{0x}^2$ and $z_{0y} = \frac{1}{2}kw_{0y}^2$ are Rayleigh ranges corresponding to the transverse scale widths, $\alpha_0 = w_{0\xi}/w_{0x}$ is the spacetime eccentricity of the STOV, and $A^{(0)}$ ensures $\langle A_{l,\alpha} | A_{l,\alpha} \rangle = \int d^2\mathbf{r}_\perp d\xi A_{l,\alpha}^* A_{l,\alpha} = 1$.

For the STOV pulse of Eq. (1) launched from vacuum into a slab of dispersive medium with dimensionless group velocity dispersion β_2 (see Appendix A), the expectation value of intrinsic electromagnetic tOAM *in the medium* per incident photon is [2]

$$\langle L_y^{EM} \rangle_{l,\alpha} = \frac{1}{2}l \left(\alpha - \frac{\beta_2}{\alpha} \right). \quad (2)$$

If the incident pulse eccentricity ratio is α_0 , then in the medium $\alpha = (v_g/c)\alpha_0$ due to the longitudinal compression of the STOV upon entering the slab, where v_g is the group velocity in the medium. As the tOAM per incident photon is $\langle L_y^{EM} \rangle_{l,\alpha} = \frac{1}{2}l\alpha_0$, Eq. (2) suggests that *the medium*

itself has taken up intrinsic tOAM $\langle L_y^{med} \rangle_{l,\alpha} = \frac{1}{2}l((\alpha_0 - \alpha) + \beta_2/\alpha)$, assuming negligible reflection. We have identified this material-based tOAM structure as a STOV polariton [2]. For a collisionless plasma of electron density N_e , the dielectric function $\varepsilon(\omega) = 1 - \omega_p^2/\omega^2$ ($= n^2$, the square of refractive index) gives a dimensionless group velocity dispersion with the particularly simple form $\beta_2 = -\omega_p^2/\omega_0^2 = -N_e/N_{cr}$, where $\omega_p = (4\pi N_e e^2/m)^{1/2}$ is the plasma frequency and $N_{cr} = m\omega_0^2/4\pi e^2$ is the critical density, and ω_0 is the central frequency. The group velocity is $v_g = c(1 - N_e/N_{cr})^{1/2}$.

Our simulations were performed using the PIC code EPOCH [16], directly solving the Maxwell-Lorentz system of equations for the EM field and for the plasma electrons and ions (protons). The dimensions of the PIC simulation grid were $100 \mu\text{m}$ (z) \times $60 \mu\text{m}$ (x), with 4096×1536 grid points. The plasma initially contained a uniform distribution of 20 macroparticles per cell of each species (protons and electrons), with each macroparticle composed of 8.15×10^7 to 1.63×10^{11} protons or electrons depending on the defined density. The device of “macroparticles” is used to achieve realistic particle densities while greatly reducing the computational load. Crucially in our simulations, ions were allowed to move. While the protons’ displacement is small compared to that of electrons owing to the high mass ratio, the laser field imparts approximately the same linear and angular momentum to both species; the proton response cannot be neglected.

The PIC simulation computes the \mathbf{E} and \mathbf{H} fields in vacuum and in the plasma as well as the positions \mathbf{r}_j and momenta \mathbf{p}_j of all the macroparticles in the plasma. The tOAM of the EM field and the plasma medium are, *per incident photon*,

$$L_y^{EM} = 2k_0 U_{inc}^{-1} \int d^2\mathbf{r}_\perp d\xi (\mathbf{r} \times (\mathbf{E} \times \mathbf{H}))_y \quad (3a)$$

$$L_y^{med} = L_{ye} + L_{yi} = 2k_0 U_{inc}^{-1} \left[\sum_j W_j (\mathbf{r}_{je} \times \mathbf{p}_{je})_y + \sum_j W_j (\mathbf{r}_{ji} \times \mathbf{p}_{ji})_y \right], \quad (3b)$$

where $U_{inc} = \int d^2\mathbf{r}_\perp d\xi (|\mathbf{E}|^2 + |\mathbf{H}|^2)$ is evaluated at $z < 0$ before the pulse encounters the entrance interface, $W_j (= 8.15 \times 10^7 \text{ to } 1.63 \times 10^{11})$ is the number of electrons or protons in a macroparticle, the index j ranges over all the electron and proton macroparticles, and the subscripts e and i refer to the electrons and ions (protons). For the symmetric STOV of this simulation, the centre of energy of the STOV pulse in vacuum and of the field-particle disturbance in the medium propagates along $\hat{\mathbf{z}}$. Therefore, choosing the origin $(x, z) = (0, 0)$ for calculation of L_y^{EM} and L_y^{med} in Eq (3) ensures that extrinsic tOAM vanishes [14] and that the tOAM calculated in Eq. (3) is intrinsic. All tOAM discussed in this paper is intrinsic.

III. RESULTS AND DISCUSSION

We first examine the normal incidence reflection of a y-polarized STOV pulse from a plasma slab with $N_e/N_{cr} = 2$, whose front face is at $z = 0$. Initially, we consider the linear case for small normalized vector potential, $a_0 = eA/mc^2 = 0.001$. We use $l = 1$, $\alpha_0 = 1$, $\lambda_0 = 800 \text{ nm}$ (for which $N_{cr} = 1.71 \times 10^{21} \text{ cm}^{-3}$), $w_{0\xi} = 10 \mu\text{m}$ (FWHM pulsewidth $\tau \sim 55 \text{ fs}$), $w_{0x} = 10 \mu\text{m}$, and $w_{0y}/w_{0x} \gg 1$ so that the field dependence in y was neglected and EPOCH was run in 2D+1 mode. This over-critical plasma density is chosen to ensure that 100% energy reflection occurs

over the full STOV bandwidth. Figure 1(a) shows the STOV pulse, launched from its waist at $z = -50 \mu\text{m}$, as it approaches the slab's front face. The direction of the $l = 1$ phase winding is shown superimposed. In Figure 1(b), the leading part of the pulse reflects from the interface as the back of the pulse is still incident; the log of the evanescent field in the skin depth is plotted at $z > 0$. The fully reflected pulse is shown in Fig. 1(c), where the phase winding has reversed: the physical reflection boundary conditions ensure that the STOV fields flip sign and the tOAM flips sign.

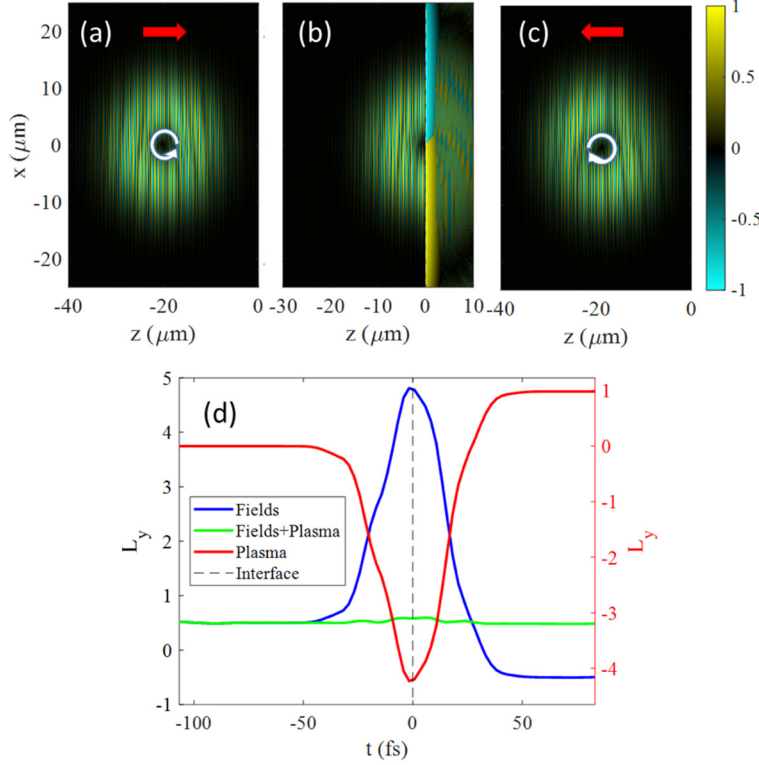


Figure 1. Conservation of total tOAM during reflection from an overcritical density plasma slab. **(a)** Propagation of an $l = 1$, $\alpha_0 = 1$, $a_0 = 0.001$ STOV pulse toward the plasma slab ($N_e/N_{cr} = 2$) with front face at $z = 0$. **(b)** Frame when STOV singularity has reached the interface, with half of the pulse reflecting and half still incident. **(c)** Pulse fully reflected from interface, with winding and tOAM flipped. The dark stripes in (a), (b), (c) are where the phase cycles to 0; they form the forked fringe pattern characteristic of vortex pulses. **(d)** Time evolution of tOAM contributions through the interaction. Units are tOAM per incident photon. The red vertical scale at the right applies to the red curve for plasma tOAM. The black vertical scale at the left applies to the other curves. The vertical black line at $t = 0$ is the time corresponding to panel (b).

The time-dependent accounting of tOAM contributions is plotted in Fig. 1(d). As the STOV propagates in vacuum in the $+\hat{z}$ direction (Fig. 1(a)), it has $+1/2$ unit of tOAM per photon (blue curve for $t < \sim -50$ fs), as predicted by our theory [2]. As the STOV interaction with the plasma begins, a transient positive spike in the EM tOAM develops, accompanied by an opposing spike associated with the plasma tOAM (red curve). The vertical dashed line marks the arrival time of the STOV singularity at the interface. After the reflection is completed ($t > \sim 40$ fs), the STOV departs in the $-\hat{z}$ direction with $-1/2$ units of tOAM per photon. However, to conserve angular momentum, the plasma is left with twice the tOAM of the incident STOV, $+1$ unit per incident photon (red curve, $t > \sim 40$ fs). The sum intrinsic tOAM of the fields and particles per incident photon is plotted as the green curve in Fig. 1(d); it remains constant at $+1/2$ throughout the interaction. For an incident STOV with $l = -1$, the spikes flip and the sum tOAM remains

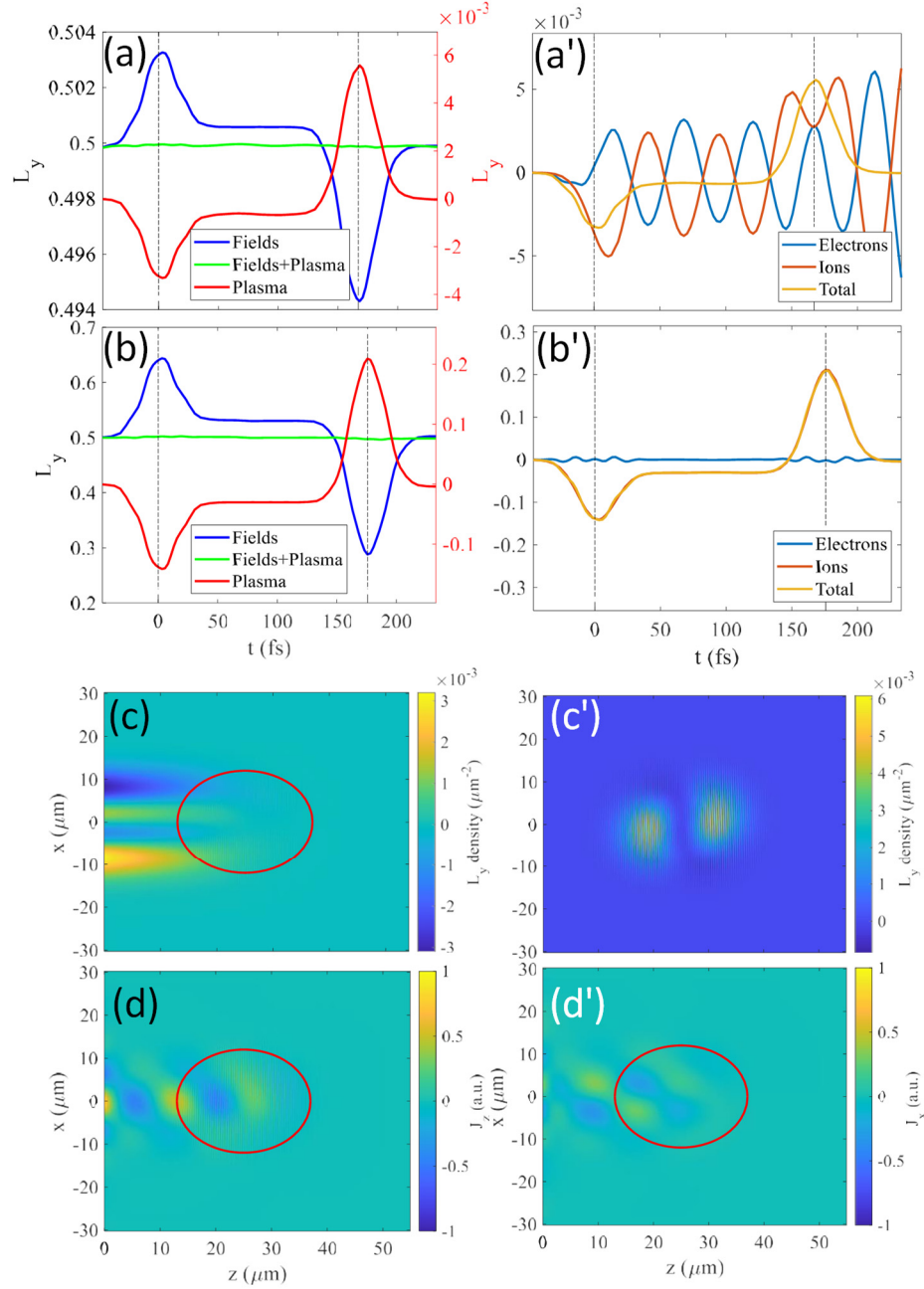


Figure 2. (a) Intrinsic tOAM of STOV pulse (linear case $a_0 = 0.001$), plasma, and their sum vs. propagation distance through a 50- μm -thick plasma slab with $N_e/N_{cr} = 0.0025$. The constant sum verifies conservation of intrinsic tOAM momentum over the particles and fields. (a') Electron and ion tOAM, and their sum (corresponding to (a)). (b) same as (a) for $N_e/N_{cr} = 0.1$. (b') Electron and ion tOAM, and their sum (corresponding to (b)). (c) tOAM density distribution of plasma. The red ellipse indicates the pulse location. (c') tOAM density distribution of STOV pulse. (d) longitudinal current density distribution j_z (d') transverse current density distribution j_x . These are proportional to pulse energy and so (d) and (d') are normalized.

constant at $-1/2$. The small fluctuations in sum tOAM near $t = 0$ are from the abrupt transition at the interface from a simulation cell with no particles to one with the full particle density. As will

be discussed later, the source of the counterbalancing interface spikes in tOAM for fields and particles is the spatiotemporal torque exerted by the light on the plasma and vice versa.

Next, we examine the same STOV pulse normally incident on a thin ($d = 50 \mu\text{m}$) subcritical density plasma slab, chosen so that $d/z_{0x} \ll 1$. The front face of the thick slab is at $z = 0$. In Fig. 2(a), for $N_e/N_{cr} = 0.0025$, the evolution of the field tOAM, the plasma tOAM (sum of electron and ion contributions), and the total tOAM is shown as the STOV propagates from vacuum, through the slab, and then exits into vacuum. At this plasma density, interface reflections are negligible. The STOV's tOAM per photon is initially $+1/2$ as it approaches the interface at $z = 0$ and then spikes as it enters the plasma (blue curve), with an equal and opposite tOAM picked up by the plasma particles (red curve). These spikes would flip for $l = -1$. As the STOV fully enters the plasma, the spikes decline and the tOAM levels off to constant values for the fields and particles. It is in this steady propagation region that we will compare simulation results with our theory [2]. As the STOV passes through the right side of the slab, a negative spike in field tOAM develops, accompanied by a positive spike in particle tOAM. Upon exit, the STOV emerges with its original $+1/2$ tOAM per photon, as the particles have returned all tOAM to the field. Throughout the propagation, the sum tOAM (green curve) remains $+1/2$.

Results for the higher density case $N_e/N_{cr} = 0.1$ are plotted in Fig. 2(b), where reflections at the front and back interface are taken into account. The form of the tOAM evolution is similar to Fig. 2(a), with counterbalancing positive and negative spikes of the field and particle contributions at the slab entrance and exit, with particle tOAM returned to the exiting pulse. However, because of the higher plasma density, the interface spikes for the fields and plasma are much larger, as are the levels of steady tOAM regions in the bulk plasma between the interfaces.

The individual responses of the electrons and ions for Fig. 2(a) and 2(b) are plotted in Fig. 2(a') and 2(b'), where it is seen that the behaviour is strongly dependent on plasma density. In the lower density case of Fig. 2(a,a'), where the pulse length is shorter than the plasma wavelength, $w_{0\xi} < \lambda_p = 2\pi c/\omega_p$, the tOAM of the electrons and ions oscillate π out of phase with similar amplitudes, exchanging tOAM at the plasma frequency ω_p . The tOAM oscillation amplitudes are similar because the driven electron and ion velocities scale as the inverse of their masses, so that their linear momentum densities and tOAM densities are similar. After the pulse exits the slab, the oscillations in electron and ion tOAM continue, but they sum to zero. In the higher density case of Fig. 2(b,b'), where $w_{0\xi} \gg \lambda_p$, any torque by the light on the electrons is immediately distributed between the electrons and ions according to their mass ratio, with ion tOAM greatly dominating. This is because the pulse is long enough for plasma electrostatic forces to pull the ions to the same velocity as electrons so that their linear momentum density and thus tOAM density contributions scale as the charge carrier mass. The sum particle tOAM, dominated by the ions, then goes to zero as the pulse exits the slab.

For a position of the STOV pulse within the bulk for $N_e/N_{cr} = 0.0025$, the particle and field tOAM densities are plotted in Figs. 2(c) and 2(c'), and the associated longitudinal and transverse current densities, j_z and j_x , are plotted in Figs. 2(d) and 2(d'). These results will be discussed later in the context of Fig. 5.

We now consider the steady tOAM of the EM field and particles during linear propagation of the STOV ($a_0 = 0.001$) in the bulk of the plasma slab away from the interfaces. The theory prediction for the STOV tOAM in the medium is $\langle L_y^{EM} \rangle = \frac{1}{2}l(\alpha - \beta_2/\alpha) = \frac{1}{2}[v_g/c +$

$(c/v_g) N_e/N_{cr}]$ for $l = 1$, $\alpha_0 = 1$, and $v_g = c(1 - N_e/N_{cr})^{1/2}$. Our theory (blue curve) and the PIC simulations (blue circles) are in excellent agreement.

For the medium response, the theory predicts $\langle L_y^{med} \rangle = \frac{1}{2}(1 - v_g/c - (c/v_g) N_e/N_{cr})$. This is plotted as L_y^{plasma} (red curve) in Fig. 3(a). The PIC simulation results for the particle tOAM (using Eq. (5b)) are plotted as the open red circles. Agreement with our theory is excellent, *confirming both the existence of STOV polaritons and the value of their tOAM*. The PIC results deviate only near critical density, where the redder frequencies in the STOV bandwidth reflect more than the blue from the entrance interface, affecting the particle tOAM. The physics of this effect is discussed later in the context of Fig. 5.

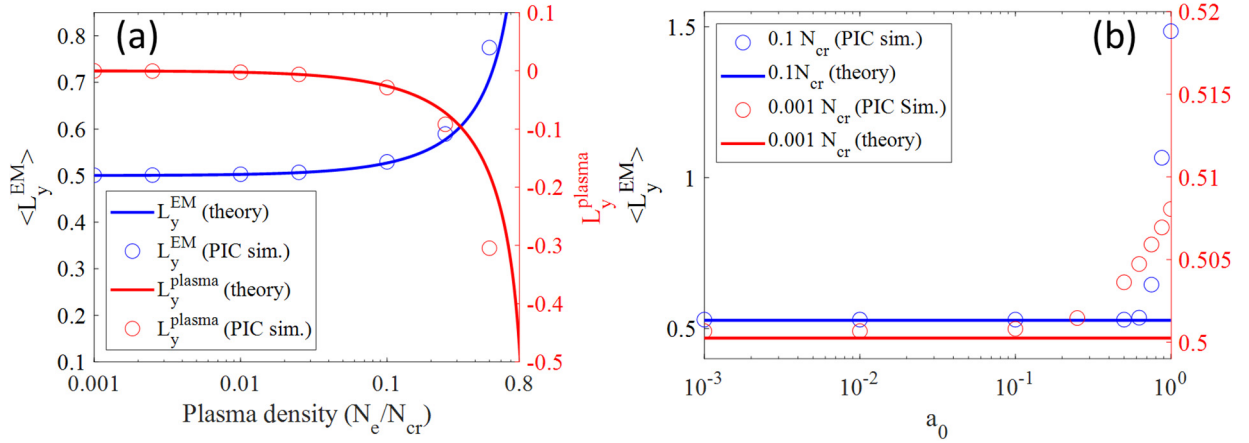


Figure 3. Comparison of tOAM linear theory [2] and PIC simulation results for varying plasma density and peak field. **(a)** Field tOAM $\langle L_y^{EM} \rangle$ and particle tOAM L_y^{plasma} per incident photon from theory (solid curves) and PIC simulation (open circles) for $a_0 = 0.001$. Deviation from theory occurs only at near-critical density, where the redder portion of the incident STOV spectrum cannot penetrate the interface. **(b)** Comparison of linear theory (solid curves) and PIC simulation predictions of $\langle L_y^{EM} \rangle$ for two densities, for a_0 ranging from linear to relativistic strength ($a_0 \sim 1$).

Up to this point, we have examined only linear propagation of STOVs in dispersive media. Figure 3(b) shows how the linear theory deviates from the PIC simulation results as a_0 is increased to relativistic levels. $\langle L_y^{EM} \rangle$ is plotted for two cases, $N_e/N_{cr} = 0.001$ and $N_e/N_{cr} = 0.1$. For the low-density case, theory matches the PIC simulation up to $a_0 \sim 0.2$, while for the higher density case it matches up to $a_0 \sim 0.7$, approaching relativistic levels. For the simulation points in Fig. 3(b) deviating from the linear theory as a_0 increases, $\langle L_y^{EM} \rangle$ begins to fluctuate with propagation owing to the excitation of collective plasma oscillations; the points are then computed as averages over the range between the interfaces. For our thin slab ($d/z_{0x} \ll 1$), there is weak relativistic self-focusing at either density, with plasma density modification occurring around the pulse body as $a_0 \rightarrow 1$ and electrons are ponderomotively pushed out of the beam. For the higher density case, this is harder to do owing to the stronger electrostatic restoring force on the electrons; hence the better fit of the linear theory for larger a_0 . Deviation occurs for both cases as the electron density local to the pulse is ponderomotively driven out and tOAM is taken up by large amplitude plasma waves.

IV. NATURE OF THE STOV POLARITON

Left unaddressed thus far is the nature of the STOV polariton, and we discuss that now. We start with and then justify the statement that *it is the combination of the ponderomotive force and material dispersion that drives the STOV polariton*. In our case, to have OAM along $\hat{\mathbf{y}}$, there must be particle linear momentum in the spatiotemporal or $x\xi$ plane. The only driver for such motion is the Lorentz force density, $\mathbf{f} = N_e(-e)\mathbf{v} \times \mathbf{B}/c$. For $a_0 \ll 1$ and in the moving coordinates (x, ξ) (see Appendix A), $\bar{\mathbf{f}} = -\nabla u$, the ponderomotive force density on the electrons, the overbar denotes cycle average and $u = N_e e^2 E_{y0}^2 / 4m\omega^2 = (16\pi)^{-1}(\omega_p^2/\omega^2)E_{y0}^2 = (16\pi)^{-1}(-\varepsilon(\omega) + 1)E_{y0}^2$ is the ponderomotive energy density. Note that ∇ rather than ∇_{ST} (see Appendix A) is used here because the plasma is stationary in the lab frame. This force can also be derived using the divergence of the electromagnetic stress tensor [17] in the plasma dielectric medium.

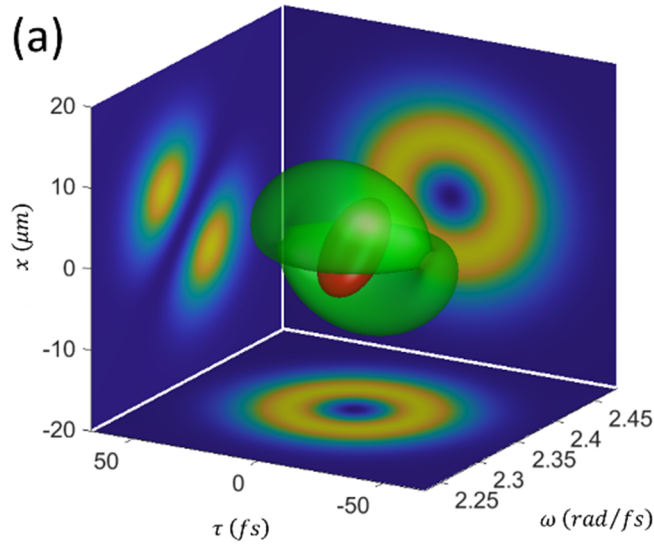


Figure 4. Wigner plot of the STOV pulse before it enters the interface and its integral projections (see Appendix B). The central object (the Wigner intensity distribution) is the 20% intensity isosurface; green depicts where the field is positive and red depicts where it is negative. The familiar spacetime STOV is seen in the $x - \tau$ projection $|E(x, \xi)|^2$ (where $\xi = v_g \tau$), its spatio-spectral representation $|\tilde{E}(x, \omega)|^2$ is the $x - \omega$ projection, and its spectral evolution is in the $\omega - \tau$ projection.

To help understand the role of dispersion, Fig. 4 presents a Wigner plot of the incident STOV pulse (see Appendix B). The $x - \tau$ projection is the familiar spacetime STOV intensity profile, $|E(x, \xi)|^2$, where $\xi = v_g \tau$. The $x - \omega$ projection is the spatio-spectral profile $|\tilde{E}(x, \omega)|^2$, which exhibits a spatio-spectral “tilt” as it enters the dispersive medium. Given that the plasma dielectric response depends on frequency, it is evident that the distribution of ponderomotive force density will be unbalanced along x , through the centre of energy of the pulse, resulting in a net torque. Plotted in Figs. 5(a) and 5(b) are maps of the y-component of torque density on the electrons, $\mathcal{T}_y(x, \xi) = (\mathbf{r} \times \bar{\mathbf{f}})_y = -(\xi \partial u / \partial x + x \partial u / \partial \xi)$, where u is the electron ponderomotive energy density taken from the PIC simulation. In Fig. 5(a), as the front part of the pulse enters the medium, but before the STOV singularity reaches the interface, the integral of the torque density is negative

(hence the negative-going spike in particle tOAM in Figs. 2(a) and 2(b)). As the singularity moves past the interface and into the bulk, the torque density integral becomes positive, the spike declines, and the particle tOAM relaxes to its steady value as the STOV moves into the bulk (Fig. 5(b)). As seen in Figs. 2(a) and 2(b), as the STOV pulse exits the slab, the opposite effects occur. In Fig. 5(c) we compare the time derivative of the plasma tOAM of Fig. 2(b), dL_y^{plasma}/dt , and the integrated torque density $T(t) = \int dx d\xi \mathcal{T}_y(x, \xi; z)$, where $t = z/v_g$. The excellent agreement supports our picture of spatiotemporal torques in dispersive media driven by ponderomotive forces.

Given this torque picture, we now examine Figs. 2(c,c') and 2(d,d'), where the STOV pulse is fully in the bulk. In Fig. 2(c), it is seen that the particle tOAM density is non-zero all the way back to the entrance interface at $z = 0$. However, its *integral* has a non-zero contribution only inside the red ellipse, which is where the torque density distribution $\mathcal{T}_y(x, \xi)$ (like that of Fig. 5(b)) increases the particle tOAM from zero to its steady value of the propagating polariton. The tOAM density of the driving STOV pulse is shown in Fig. 2(c'). The x - and z - components of the current density driven by $\mathcal{T}_y(x, \xi)$ are plotted in Figs. 2(d) and 2(d'). It is these components which contribute to net polariton tOAM, but only where $\mathcal{T}_y(x, \xi)$ is non-zero.

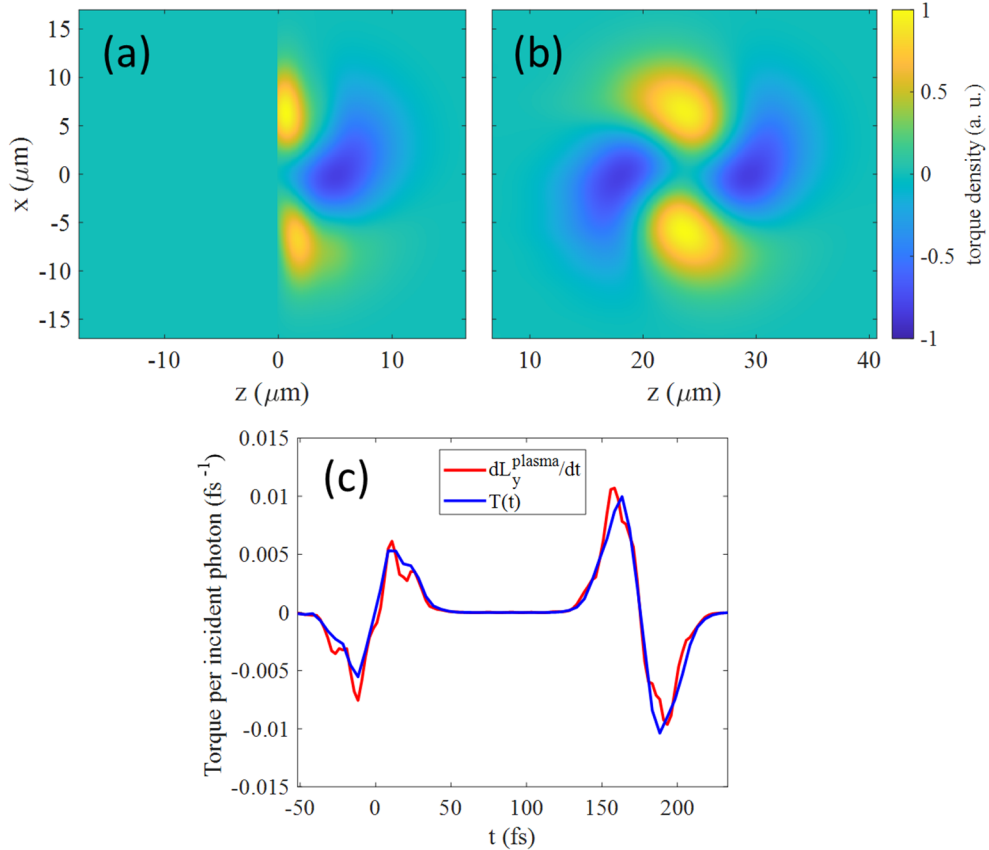


Figure 5. (a) Torque density on electrons just before the STOV singularity reaches the front interface. (a') Torque density on electrons when the STOV is entirely inside the slab. The plasma density is $N_e/N_{cr} = 0.1$ and $a_0 = 0.001$. (b) and (b') are normalized since torque density $\mathcal{T}_y(x, \xi)$ scales linearly with pulse energy. (b) Plots of time derivative of the plasma tOAM of Fig. 2(b), dL_y^{plasma}/dt , and of integrated torque density $T(t) = \int dx d\xi \mathcal{T}_y(x, \xi; z)$, where here $t = z/v_g$.

Finally, we note that for a general uniform dielectric medium characterized by a dielectric function $\varepsilon(\omega)$, it can be shown that the bound current driven by the ponderomotive force leads to the medium tOAM per photon of $\langle L_y^{med} \rangle = \frac{1}{2}l \beta_2 / \alpha$.

V. CONCLUSIONS

We have verified the existence of the STOV polariton and the value of its transverse orbital angular momentum, in agreement with our theory [2]. The polariton and its transverse OAM are excited by torques imposed by light pressure forces in a dispersive medium. To verify our theory and obtain physical insight, we used a first principles particle-in-cell simulation-- depending only on Maxwell's equations and the Lorentz force-- of a simple dispersive medium, a fully ionized hydrogen plasma. The polariton co-propagates with the pulse while taking up tOAM from it, and then returns the tOAM to the pulse upon its exit from the medium. In an absorbing medium, we would expect mass rotation around the tOAM axis. In a plasma, the tOAM is taken up in two distinct regimes: (a) nearly equally shared and oscillatory between electrons and ions for the STOV pulse shorter than the plasma wavelength, and (b) nearly entirely taken up by the ions when the pulse is much longer than the plasma wavelength. The linear theory is applicable across a wide range of plasma density and STOV field strength.

This work is supported by the Air Force Office of Scientific Research (FA9550-21-1-0405) and the US Department of Energy (DE-SC0024398 and DE-SC0024406).

APPENDIX A: REVIEW OF TRANSVERSE OAM THEORY

To briefly review, the linear theory finds modal solutions in dispersive media to the spatiotemporal paraxial wave equation,

$$2ik_0 \partial \mathbf{A} / \partial z = (\nabla_{\perp}^2 + \beta_2 \partial^2 / \partial \xi^2) \mathbf{A} = H \mathbf{A} , \quad (\text{A1})$$

where $\mathbf{A} = \mathbf{A}(\mathbf{r}_{\perp}, \xi; z)$ is the propagating field, \mathbf{r}_{\perp} represents coordinates transverse to the propagation direction $\hat{\mathbf{z}}$, ∇_{\perp}^2 is the transverse Laplacian, H is the propagation operator, $k_0 = k(\omega_0)$ is the pulse central wavenumber, $\xi = v_g t - z$ is a space coordinate local to the pulse, $v_g = (\partial k / \partial \omega)^{-1}_{\omega_0}$ is the pulse group velocity, $\beta_2 = v_g^2 k_0 k_0''$ is the dimensionless group velocity dispersion (GVD), and the argument z is separated by a semicolon it plays the role of a timelike running parameter.

The modal solutions derived in [2] are $A_{mpq}(x, y, \xi; z) = A_{mpq}^{(0)} u_m^x(x; z) u_p^y(y; z) u_q^{\xi}(\xi; z)$, where $u_m^x(x; z) = C_m w_x^{-1/2}(z) H_m\left(\frac{\sqrt{2}x}{w_x(z)}\right) e^{-x^2/w_x^2(z)} e^{ik_0 x^2/2R_x(z)} e^{-i(m+1/2)\psi_x(z)}$ and $u_p^y(y; z)$ (with similar form) are standard Hermite-Gaussian functions with $C_m = (2/\pi)^{1/4} (2^m m!)^{-1/2}$, H_m is a Hermite polynomial of order m , $w_x(z) = w_{0x}(1 + (z/z_{0x})^2)^{1/2}$, $R_x(z) = z(1 + (z_{0x}/z)^2)$ and $\psi_x(z) = \arctan(z/z_{0x})$. Meanwhile, $u_q^{\xi}(\xi; z) = C_q w_{\xi}^{-1/2}(z) H_q\left(\frac{\sqrt{2}\xi}{w_{\xi}(z)}\right) e^{-\xi^2/w_{\xi}^2(z)} e^{-ik_0 \xi^2/2\beta_2 R_{\xi}(z)} e^{i(q+1/2)\psi_{\xi}(z)}$, where $C_q =$

$(2/\pi)^{1/4}(2^q q!)^{-1/2}$, H_q is a Hermite polynomial of order q , $w_\xi(z) = w_{0\xi}(1 + (z/z_{0\xi})^2)^{1/2}$, $R_\xi(z) = z(1 + (z_{0\xi}/z)^2)$, $\psi_\xi(z) = \text{sgn}(\beta_2) \arctan(z/z_{0\xi})$, and $z_{0\xi} = k_0 w_{0\xi}^2/2|\beta_2|$.

Any spatiotemporal field can be constructed as a linear combination of these spatiotemporal Hermite Gaussian (STHG) modes A_{mpq} . Azimuthal STOV modes of winding number l (such as in Eq. (1)) can be represented in the STHG basis as [23]

$$\text{STOV}_{0l}(x, y, \xi; z) = \sum_j^{|l|} C_j A_{j,0,|l|-j}(x, y, \xi; z), \quad (\text{A2})$$

where $C_j = (|l|/(2j)!(|l| - j)!)[(|l| - 2j)!(2j)!/2^{|l|}|l|!]^{1/2}$. Radial STOV modes can be constructed in a similar manner.

In ref. [2], conservation of EM energy density flux leads to identification of the spacetime linear momentum operator $\hat{\mathbf{p}}_{ST}$ and the tOAM operator L_y :

$$\hat{\mathbf{p}}_{ST} = -i\nabla_{ST} = -i(\nabla_\perp - \hat{\xi}\beta_2\partial/\partial\xi), \quad (\text{A3a})$$

$$L_y = (\mathbf{r} \times \hat{\mathbf{p}}_{ST})_y = -i\left(\xi\frac{\partial}{\partial x} + \beta_2 x\frac{\partial}{\partial \xi}\right), \quad (\text{A3b})$$

Furthermore, because the operators H and L_y commute, $[H, L_y] = 0$, the expectation value $\langle L_y \rangle = \langle A|L_y|A \rangle = \int d^2\mathbf{r}_\perp d\xi A^* L_y A$ of L_y is conserved with propagation: $d/dz \langle L_y \rangle = i(2k_0)^{-1} \langle [H, L_y] \rangle = 0$. If $\langle L_y \rangle$ is calculated with respect to the pulse center of energy (or energy centroid), it is the *intrinsic* tOAM [14], a property of photons. In this paper, we consider only intrinsic tOAM.

APPENDIX B: WIGNER FIELD DISTRIBUTION

The Wigner Field Distribution (WFD) gives the spectral composition of a signal as function of time [24]

$$\text{WFD}(t, \omega) = \int_{-\infty}^{\infty} d\tau f\left(t + \frac{\tau}{2}\right) f^*\left(t - \frac{\tau}{2}\right) e^{-i\omega\tau}. \quad (\text{A4})$$

It is straightforward to extend this to an electric field with spatial dependence to obtain the WFD as a function of $\{x, y, \xi, \omega\}$:

$$\text{WFD}(x, y, \xi, \omega) = \frac{1}{v_g} \int_{-\infty}^{\infty} d\xi' f\left(x, y, \xi + \frac{\xi'}{2}\right) f^*\left(x, y, \xi - \frac{\xi'}{2}\right) e^{-i\omega\xi'/v_g}. \quad (\text{A5})$$

REFERENCES

- [1] N. Jhajj, I. Larkin, E. W. Rosenthal, S. Zahedpour, J. K. Wahlstrand, and H. M. Milchberg, *Spatiotemporal Optical Vortices*, Phys. Rev. X **6**, 031037 (2016).
- [2] S. W. Hancock, S. Zahedpour, and H. M. Milchberg, Mode Structure and Orbital Angular Momentum of Spatiotemporal Optical Vortex Pulses, Phys. Rev. Lett. **127**, 193901 (2021).

- [3] L. Allen, M. W. Beijersbergen, R. J. C. Spreeuw, and J. P. Woerdman, *Orbital angular momentum of light and the transformation of Laguerre-Gaussian laser modes*, Phys. Rev. A **45**, 8185 (1992).
- [4] M. S. Le, G. A. Hine, A. Goffin, J. P. Palastro, and H. M. Milchberg, *Self-Focused Pulse Propagation Is Mediated by Spatiotemporal Optical Vortices*, Phys. Rev. Lett. **133**, 053803 (2024).
- [5] K. Y. Bliokh and F. Nori, *Spatiotemporal vortex beams and angular momentum*, Phys. Rev. A **86**, 033824 (2012).
- [6] N. Jhajj, *Hydrodynamic and Electrodynamical Implications of Optical Femtosecond Filamentation*, Ph.D. Dissertation, University of Maryland, 2017.
- [7] S. Zahedpour, S. W. Hancock, and H. M. Milchberg, *Direct Measurement of Linearly Imposed Spatiotemporal Optical Vortices (STOVs)*, in *Frontiers in Optics + Laser Science APS/DLS (2019), Paper FW5F.5* (Optica Publishing Group, 2019), p. FW5F.5.
- [8] S. W. Hancock, S. Zahedpour, A. Goffin, and H. M. Milchberg, *Free-space propagation of spatiotemporal optical vortices*, Optica, OPTICA **6**, 1547 (2019).
- [9] G. Gui, N. J. Brooks, H. C. Kapteyn, M. M. Murnane, and C.-T. Liao, *Second-harmonic generation and the conservation of spatiotemporal orbital angular momentum of light*, Nat. Photon. **15**, 608 (2021).
- [10] A. Chong, C. Wan, J. Chen, and Q. Zhan, *Generation of spatiotemporal optical vortices with controllable transverse orbital angular momentum*, Nat. Photonics **14**, 350 (2020).
- [11] H. Wang, C. Guo, W. Jin, A. Y. Song, and S. Fan, *Engineering arbitrarily oriented spatiotemporal optical vortices using transmission nodal lines*, Optica, OPTICA **8**, 966 (2021).
- [12] V. B. Novikov and T. V. Murzina, *Nonlocality-mediated spatiotemporal optical vortex generation in nanorod-based epsilon-near-zero metamaterials*, Opt. Lett., OL **48**, 2134 (2023).
- [13] S. W. Hancock, S. Zahedpour, and H. M. Milchberg, *Second-harmonic generation of spatiotemporal optical vortices and conservation of orbital angular momentum*, Optica, OPTICA **8**, 594 (2021).
- [14] S. W. Hancock, S. Zahedpour, A. Goffin, and H. M. Milchberg, *Spatiotemporal Torquing of Light*, Phys. Rev. X **14**, 011031 (2024).
- [15] S. W. Hancock, N. Tripathi, M. S. Le, A. Goffin, and H. M. Milchberg, *Transverse Orbital Angular Momentum of Amplitude-Perturbed Fields*, arXiv:2411.07209.
- [16] T. D. Arber et al., *Contemporary particle-in-cell approach to laser-plasma modelling*, Plasma Phys. Control. Fusion **57**, 113001 (2015).
- [17] J. D. Jackson, *Classical Electrodynamics*, 2nd ed. (Wiley, New York, 1975).
- [18] F. Sun, W. Wang, H. Dong, J. He, Z. Shi, Z. Lv, Q. Zhan, Y. Leng, S. Zhuang, and R. Li, *Generation of isolated attosecond electron sheet via relativistic spatiotemporal optical manipulation*, Phys. Rev. Research **6**, 013075 (2024).
- [19] A. E. Willner, K. Pang, H. Song, K. Zou, and H. Zhou, *Orbital angular momentum of light for communications*, Applied Physics Reviews **8**, 041312 (2021).
- [20] C. Paterson, *Atmospheric Turbulence and Orbital Angular Momentum of Single Photons for Optical Communication*, Phys. Rev. Lett. **94**, 153901 (2005).
- [21] Y. Fang, S. Lu, and Y. Liu, *Controlling Photon Transverse Orbital Angular Momentum in High Harmonic Generation*, Phys. Rev. Lett. **127**, 273901 (2021).

- [22] Y. Wu, Z. Nie, F. Li, C. Zhang, K. A. Marsh, W. B. Mori, and C. Joshi, *Spatial and Spatiotemporal Vortex Harmonics Carrying Controllable Orbital Angular Momentum Generated by Plasma Mirrors*, in *Optica Nonlinear Optics Topical Meeting 2023 (2023)*, Paper M2B.6 (Optica Publishing Group, 2023), p. M2B.6.
- [23] I. Kimel and L. R. Elias, *Relations between Hermite and Laguerre Gaussian modes*, IEEE Journal of Quantum Electronics **29**, 2562 (1993).
- [24] P. Flandrin, *Time-Frequency/Time-Scale Analysis*, Elsevier, 1998 Chapter 3.2